Review of Scientific Instruments

RESEARCH ARTICLE | JUNE 03 2026

Implementation of radio-frequency magnetic fields for electron spin resonance in a low-temperature atomic force microscope

Raffael Spachtholz ; Lisanne Sellies ; Franziska Bruckmann ; Philipp Scheuerer ; Jascha Repp

Rev. Sci. Instrum. 97, 063704 (2026)
https://doi.org/10.1063/5.0327676

Review of Scientific Instruments ARTICLE pubs.aip.org/aip/rsi

Implementation of radio-frequency magnetic fields for electron spin resonance in a low-temperature atomic force microscope

Cite as: Rev. Sci. Instrum. 97, 063704 (2026); doi: 10.1063/5.0327676
Submitted: 12 February 2026 • Accepted: 24 April 2026 •
Published Online: 3 June 2026

Raffael Spachtholz,[a] Lisanne Sellies,[b] Franziska Bruckmann, Philipp Scheuerer, and Jascha Repp[a]

AFFILIATIONS

Institute of Experimental and Applied Physics, University of Regensburg, 93053 Regensburg, Germany

[a]**Authors to whom correspondence should be addressed:** Raffael.Spachtholz@ur.de and Jascha.Repp@ur.de
[b]**Present address:** IBM Research, 8803 Rüschlikon, Switzerland.

ABSTRACT

The implementation of electron spin resonance in scanning tunneling microscopy (ESR-STM) represented a milestone in controlling spin systems at atomic scales. To drive spin resonance, a radio-frequency (RF) magnetic field is required. Yet, so far, in ESR-STM, instead of an RF magnetic field an RF electric field has been used for driving, which translates into an effective RF magnetic field. For cases in which such a field-conversion mechanism is not feasible, we developed an implementation of a low-GHz RF magnetic field in a scanning-probe setup. To this end, we utilized a single-loop coil based on a flexible polyimide printed-circuit-board to generate the RF magnetic field. To locally enhance the RF magnetic field in the scanning-probe junction, we used a gold-microstrip on an insulating support as a sample surface. We found that up to 3 GHz, the transmission only moderately depends on frequency and exhibits no sharp resonances. This development enabled the implementation of ESR in atomic force microscopy, as was demonstrated for individual pentacene molecules.

I. INTRODUCTION

Combining the outstanding spatial resolution of scanning probe microscopy (SPM) with electron spin resonance (ESR) enables quantum control of a single spin.[1] This achievement opened the pathway to coherent spin manipulations[2] and even quantum logic operations[3] at the single atom level with atomic-scale spatial resolution. Whereas these works were based on implementing ESR in scanning tunneling microscopy (STM),[1] recently, ESR was combined with atomic force microscopy (AFM).[4] This enabled investigations of electron-spin transitions of single molecules on insulating surfaces. By detecting spin transitions via forces, not requiring an electrical tip–sample current, ESR-AFM extends spin-sensitive measurements to systems and substrates that are inaccessible to ESR-STM. Thereby, some sources of decoherence, such as scattering with the tunneling electrons,[5] are eliminated, enabling considerably longer spin-coherence times.

A central challenge in implementing ESR-AFM lies in the generation and control of radio-frequency (RF) magnetic fields at the tip position. Most ESR experiments rely on the Zeeman splitting of unpaired electrons by means of a static magnetic field. To acquire a resonance spectrum, either the RF frequency is kept constant while the static magnetic field is swept, or vice versa. Both options were demonstrated in ESR-STM.[1,6] For states with a spin that is larger than 1/2, dipole–dipole interaction typically leads to a splitting of the spin states at zero magnetic field, enabling ESR investigations also in the absence of an external magnetic field[7]—as was used in ESR-AFM. Typical zero-field splittings in individual molecules correspond to resonances in the frequency range of 0.1–4.7 GHz.[8] However, in specific classes of molecules, notably nitrenes and carbenes, the splitting can increase substantially and reach values on the order of several tens of gigahertz.

In ESR-STM, the RF magnetic field is provided indirectly by coupling an RF electric field into the STM junction. The latter can

be achieved by adding an RF component to the otherwise static bias voltage across the junction. The RF voltage is either electrically added to the static bias[1,9] or coupled through space via a nearby antenna.[6] Together with the spin-polarization of the tip, the RF electric field translates into an effective magnetic field acting on the spin system in the junction[1,10]—a scheme that is not directly transferable to an AFM setup with a tip that is not spin polarized. Direct generation of RF magnetic fields in scanning-probe instruments has been explored in several contexts. In alternating-current STM, RF excitation has been achieved using loop antennas positioned in proximity to the tunneling junction.[11,12] In magnetic resonance force microscopy, RF fields have been produced using a microstrip,[13] a small coil,[14,15] or their combination.[16]

In this study, we followed a similar approach and directly generated an RF magnetic field in an SPM setup using the combination between a single-loop coil and a microstrip. We designed an RF circuit scheme that enables the generation of RF magnetic fields over the low-GHz frequency range, well-suited for ESR-AFM. We characterize the spectral signal-to-drive transfer function of the RF circuit ending in the single-loop coil. The microstrip sample design was used to locally enhance the magnetic field, enabling coherent spin driving along multiple spatial directions. The enhancement is estimated and compared with the magnetic field amplitudes inferred from the measured ESR-AFM Rabi frequencies.[4]

II. DESIGN CONSIDERATIONS AND IMPLEMENTATION

A. Microscope setup

The instrument used for the implementation of ESR-AFM is an in-house built STM/AFM based on a Besocke-type scanner[17,18] equipped with a qPlus sensor[19] in which the tip is scanned relative to a stationary sample surface. The microscope is suspended from springs attached to the bath cryostat, operating at liquid-helium temperature, to ensure effective mechanical decoupling. The microscope is operated under ultra-high vacuum (UHV) conditions.

B. Circuit overview

A schematic overview of the RF circuit is shown in Fig. 1. The RF signal is fed into the UHV system via a Sub-Miniature version A (SMA) feedthrough and transmitted through a semi-rigid stainless steel coaxial cable (abbreviated as coaxial cable, Art.: SC-033/50-AuSS-SS, Coax Japan Co. Ltd.) to the base of the liquid-helium bath cryostat. The signal is transmitted via an internal SMA connector to a custom-designed flexible printed-circuit-board (abbreviated as flex PCB, Beta LAYOUT Ltd.). A 1:1 unbalanced-to-balanced transmission line transformer (balun, Art.: MABA-011108, MACOM) is implemented on the board to achieve differential signal transmission, more details of which are provided in Sec. II E. The flex PCB terminates in a single-loop coil, where the magnetic field is generated.

C. Microstrip RF transmission

A flexible RF transmission line from the bath cryostat to the sample is required to preserve effective mechanical decoupling between the cryostat base plate and the SPM head (where the sample is located) and, therefore, minimize the transmission of vibrational

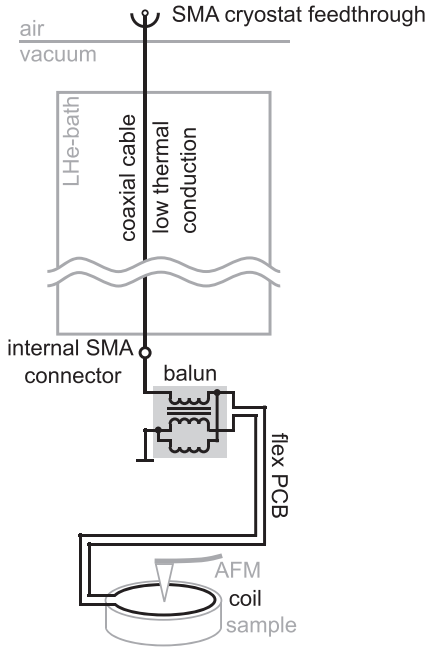

FIG. 1. Schematic of the RF circuit. The RF signal is fed into the system via an SMA feedthrough. A semi-rigid stainless steel coaxial cable with low thermal conductance transmits the signal through the helium-bath cryostat. At the bottom of the cryostat, another SMA connector couples to a Kapton®-based flexible PCB, leading the signal to the microscope head. An unbalanced-to-balanced transmission line transformer (balun) is mounted to the PCB, symmetrizing the signal, which is subsequently transmitted through a microstrip differential pair and terminates at a customized single-loop coil. The latter is also realized in the PCB and placed in the sample plane.

noise. We therefore choose to embed the transmission line in a Kapton based flex PCB. The flex PCB has a total width of 1 mm, a thickness of 0.2 mm, and a length of 25.4 cm. It was routed with twists so that the soft-bending direction changes along the transmission line, allowing for overall mechanical flexibility in all three spatial dimensions.

The embedded transmission line was implemented as a microstrip differential pair, and its cross section is illustrated in Fig. 2(a). We did an *a priori* impedance estimate with online calculation tools and designed the cross section accordingly. The resulting differential impedance was determined to be roughly 82 Ω, which differs from the 50 Ω differential impedance of the balun output—probably due to model limitations and fabrication details. Of course, an impedance match between the transmission line and the balun would be preferential and can be improved by adjustments of the transmission line dimensions or the impedance of the balun output. Reducing the Kapton thickness between the signal lines and ground line by a factor of two would bring impedance into the target range and would even improve PCB flexibility.

We derived the impedance of the transmission line from vector network analyzer (VNA) measurements of the spectrally resolved reflection S_{11} of a test transmission line of identical geometry, terminated with different terminating load resistors. The VNA was calibrated using a Short-Open-Load-Thru (SOLT) scheme. The results

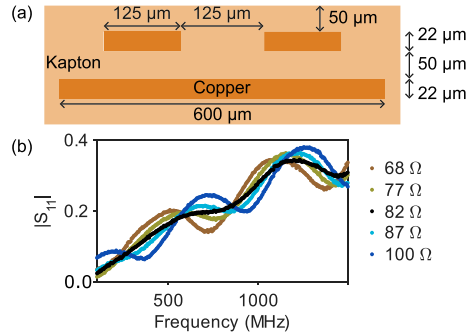

FIG. 2. (a) Cross-sectional view of the microstrip differential pair implemented in the flex PCB. (b) Reflection S_{11} measurement of the microstrip differential pair terminated with different load resistors between the two signal tracks. The test-transmission line of 12.5 cm length was connected via a 1:1 unbalanced-to-balanced transmission line transformer to the single-ended output of a VNA.

of the measurements are shown in Fig. 2(b). S_{11} shows an overall rising trend with increasing frequency due to the impedance mismatch between the transmission line and the balun output. Furthermore, the reflection shows an oscillatory behavior, which can be attributed to signal reflection at the end of the line, i.e., at the terminating load resistor. This reflection is minimized when the load resistor is matched to the impedance of the line, which we observed for values around 82 Ω.

D. Coil impedance considerations

The coil forms the termination of the flex PCB. The microstrip differential pair splits up and forms the coil, whereas the ground line ends at the coil. The coil has an imaginary frequency-dependent impedance component given by

$$X_{\mathrm{coil}} = i\omega L_{\mathrm{coil}} = i2\pi f L_{\mathrm{coil}}, \tag{1}$$

where L_{coil} is the inductance of the loop and f is the frequency. Together with the inevitable direct-current (DC) resistance R_{coil}, the coil's impedance reads

$$Z_{\mathrm{coil}} = R_{\mathrm{coil}} + i2\pi f L_{\mathrm{coil}}. \tag{2}$$

Hence, an impedance mismatch between the transmission line and the coil is unavoidable but critical for the signal-to-drive ratio, as will be discussed in the following.

The magnetic flux density generated by the single-loop coil is directly proportional to the current I_{coil} carried by the coil, with

$$I_{\mathrm{coil}} = \frac{V_{\mathrm{coil}}}{Z_{\mathrm{coil}}} = \frac{V_{\mathrm{coil}}}{R_{\mathrm{coil}} + i\omega L_{\mathrm{coil}}}, \tag{3}$$

where V_{coil} is the voltage across the coil. Hence, Z_{coil} should be minimized to maximize I_{coil}. However, for a more quantitative consideration, it is important to note that V_{coil} is not just given by the driving signal, but it depends on the boundary condition at the coil and, hence, on Z_{coil}. To define the signal-to-drive ratio, I_{coil} should be expressed solely as a function of the incident signal, that is, the forward propagating driving signal V_{drive}. To this end, we model the coil to be directly attached to a signal source as its Thevenin equivalent, which yields the expression

$$I_{\mathrm{coil}} = \frac{2V_{\mathrm{drive}}}{Z_0 + Z_{\mathrm{coil}}} = \frac{2V_{\mathrm{drive}}}{Z_0 + R_{\mathrm{coil}} + i\omega L_{\mathrm{coil}}}, \tag{4}$$

where $Z_0 = 50\ \Omega$ is the circuit impedance, and the factor of two is a consequence of the Thevenin representation of the source. Here, R_{coil} is negligible against Z_0 and will be disregarded in the following. This equivalent circuit represents a first-order RL-low-pass filter with a cutoff frequency of $f_c = Z_0/(2\pi L_{\mathrm{coil}})$. For a single-loop coil with radius r_{coil}, the inductance L_{coil} is approximately

$$L_{\mathrm{coil}} \simeq \mu_0 \pi r_{\mathrm{coil}}, \tag{5}$$

where μ_0 is the vacuum permeability.[20] For illustration, a coil of radius $r_{\mathrm{coil}} = 5$ mm gives a cutoff frequency of ~0.4 GHz. Operated at $f = 1$ GHz, the coil has an inductive impedance of $Z_{\mathrm{coil}}/i \simeq 124\ \Omega$. Hence, for the typical parameters of the given experiment, namely, a few-mm-sized coil in the low-GHz regime, one operates above the cutoff, and the signal-to-drive ratio is inversely proportional to both frequency and loop radius. In this regime, the signal-to-drive ratio cannot simply be improved by utilizing a multi-turn coil: the gain in field-per-current is outweighed by an increase in Z_{coil}, resulting in a decrease of I_{coil}.

In addition, for a given I_{coil}, the magnetic flux density in the center of a single loop is inversely proportional to the radius of the loop.[21] Hence, minimizing the radius of the loop increases the signal-to-drive ratio in two ways. Still, we choose a relatively large $r_{\mathrm{coil}} = 5$ mm, due to geometric considerations related to the size of the AFM cantilever and the necessity to move the tip across the sample. Concerning minimizing r_{coil}, we see room for improvement, in particular by designing a scan head optimized for this purpose.

Interestingly, a balun with a different impedance ratio, such as 1:2, could be used to improve the signal-to-drive ratio if $Z_{\mathrm{coil}} \gg Z_0$, as it is in our case. In this way, the impedance at the secondary side can be increased to better match that of the coil while simultaneously increasing the voltage over the secondary side and, hence, the one applied to the coil. In the geometry used here, this would require adapting the impedance of the flex PCB accordingly. Alternatively, a second RF transformer directly in front of the coil could be implemented for this purpose.

E. Balanced signal transmission

In a first design iteration, the signal was fed to the coil in a single-ended configuration. This resulted in large stray fields of the RF signal around the flex PCB, causing appreciable problems. One of them was an increase in the temperature of the SPM head (see Sec. II F) when driving the coil. We further observed artifactual signals in our SPM setup, which we attribute to a capacitive coupling, partly in conjunction with rectification effects (also Sec. II F).

In addition, the RF stray field induced twice an electrical short between an electrode of a piezoelectric element and ground—very much to our surprise. The short occurred at the edge of the electrodes closest to the flex PCB; this is why we attribute it to the RF stray field.

To minimize these issues, we switched to differential signal propagation by introducing the balun. Even with the balun present, we observed artifactual signals from the remaining stray RF electric

field. We note that an amplitude and phase imbalance of the balun may contribute to the remaining stray RF electric field, which could be minimized by using a differential signal generator instead of a balun.

F. Effects of RF generated heating and electric field on ESR-AFM

To ensure that the remaining electric field and temperature increase due to the RF transmission do not affect the resulting ESR-AFM spectra, we determined a frequency dependent limit on the allowed RF power.

The ESR-AFM experiments are performed on individual molecules in repeated cycles of spin preparation, spin manipulation, and readout.[4] The actual spin manipulation is the only phase during which the RF signal is required and accounts for only a small fraction of the total time. Although the extended readout time slows down measurements, it is fortunate in terms of limiting the thermal load: we could minimize the RF power dissipation and concomitant heating by pulsing the RF field without losing any ESR signal intensity. Hence, the RF signal was only applied during the period in which the molecule's spin state was manipulated. For a given RF pulse duration and frequency, the maximum RF power used was chosen such that the heating induced drift was negligible on the scale of the piezo creep present.

As an example, in the case of pentacene-d_{14}, we turned on our RF pulses 320 times per second, with a duration of 100 μs for taking an ESR-AFM spectrum (3% of the total time) and with a duration of up to 30 μs to measure Rabi oscillations.[4] To measure Rabi oscillations of the T_x–T_z transition around 1540 MHz, we applied an RF power of 1.75 W to the SMA cryostat feedthrough during the RF pulses. In case of the ESR-AFM spectra, we typically applied 2 to 3 orders of magnitude smaller RF powers to minimize RF power broadening.[4,22]

Next to minimizing RF induced heating, we ensured that the stray RF electric field did not lead to ESR-AFM signal distortions. In the current implementation of ESR-AFM,[4] single-electron tunneling events between the tip and the molecule are used to initialize and read out the spin state. These tunneling events are steered by a gate voltage.[23] The RF signal of the transmission line and coil is capacitively coupled to the gate voltage, which could steer undesired tunneling events. To avoid significant modulation of the gate voltage, a frequency-dependent upper limit for the RF power was determined. This limit was set such that at a gate voltage corresponding to the charge degeneracy point,[23] no RF-pulse-induced interconversion between the charge states was observed (at the tip–sample height used for the ESR-AFM measurements).

III. CHARACTERIZING THE SIGNAL TRANSMISSION

It is highly beneficial for ESR-AFM if the signal-to-drive ratio is roughly constant over the frequency ranges spanned by the resonance peak shapes (typically less than 10 MHz). The magnitude, broadening[22] and, in some cases, even the line shape[24] of zero-field triplet state ESR signals depend on the applied RF power. A variation of the signal-to-drive ratio over the frequency range of the ESR signal could thus lead to distortions in the line shape, which could be misinterpreted as features of the spin system itself.

A. Measurements of the signal transmission

Figure 3(a) shows a schematic of the setup to characterize the signal-to-drive ratio of our RF circuit using a VNA. To this end, we were picking up the RF magnetic field with an RF magnetic

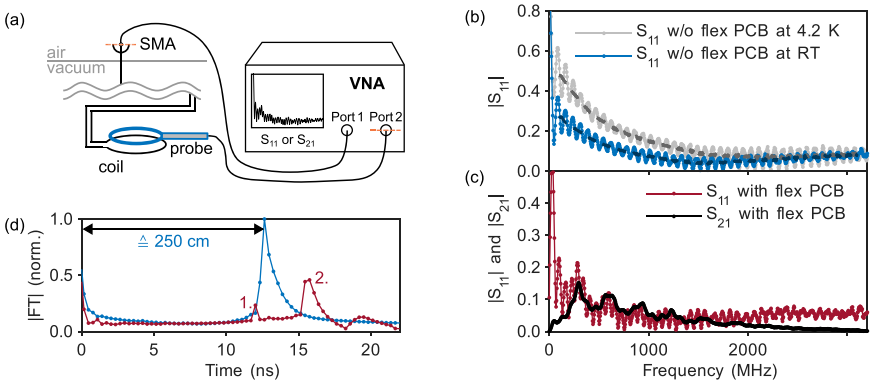

FIG. 3. (a) Schematic of the VNA-based transmission S_{21} measurements, in which port 1 was connected to the cryostat's input port, whereas port 2 was used to receive the signal from a calibrated magnetic-field probe. The VNA was calibrated using the Short-Open-Load-Thru (SOLT) scheme, with the calibration reference planes schematically indicated by dashed orange lines. In the case of the reflection S_{11} measurements, only port 1 was used, and the magnetic field probe was removed. (b) Reflection (S_{11}) measurements of the open-ended coaxial cable (flex PCB detached) at room temperature and at 4.2 K. The dashed lines show data filtered in the Fourier domain to illustrate the frequency-dependent damping of the reflected signal. (c) Reflection (S_{11}) of the RF circuit with the flex PCB connected (red trace) and transmission measurement (S_{21}) of the entire RF circuit as shown in (a) (black curve); both measured at room temperature. (d) Fourier transform (FT) of the S_{11} reflection measurements, using the same color code as in (b) and (c). Distinct peaks in the S_{11}-derived signal reveal reflection points within the RF circuit, where the associated delay time scales with the distance to the reflection point. The measurement with the open-ended coaxial cable exhibits a prominent peak at 12.6 ns, corresponding to twice the length of the cable, 125 cm. Based on this reference signal, the peaks can be assigned as due to (1) signal reflection at the balun and (2) signal reflection at the coil. Since the phase information is not essential for the transfer-function analysis of the apparatus, it is neglected; accordingly, panels (b) and (c) show the magnitude of S_{11} and S_{21}, respectively, while panel (d) displays the Fourier transform of the complex-valued signal.

field probe, the signal of which we characterized in a forward-transmission (S_{21}) measurement. Since the measurements with the RF magnetic field probe can only be performed with the cryogenic shields opened, these measurements had to be performed at room temperature. In contrast, reflection (S_{11}) measurements can be performed at room and cryogenic temperatures and provide complementary insight.

First, we measured the spectrally resolved reflection S_{11} [see Fig. 3(b)] of the open-ended (flex PCB detached) coaxial cable guided through the cryostat. S_{11} is dominated by the echo at the cryostat's bottom SMA port. Perfect transmission at the SMA feedthrough, no damping, and perfect reflection at the open end would result in $|S_{11}| = 1$ for all frequencies. Frequency-dependent damping in the coaxial cable gives rise to the overall decay trend of the curve, whereas non-perfect transmission at the SMA feedthrough leads to the oscillations in $|S_{11}|$. A Fourier transform of S_{11} brings it into the time domain [blue curve in Fig. 3(d)]. The strong peak in the Fourier transform of S_{11} is related to propagation between the open end and the SMA feedthrough and can be used to gauge the propagation delay (corresponding to twice the known cable length of 125 cm). The oscillations seen in S_{11} are similar for room and cryogenic temperatures, except for a frequency-dependent damping. The frequency-dependent damping in the coaxial cable can be directly read off from the overall decay of $|S_{11}|$ [highlighted by the dashed trend lines in Fig. 3(b)]. For example, the trend line measured at 4.2 K indicates a signal reduction by a factor of 5 after a complete forward–backward propagation cycle through the cable at 0.7 GHz, which relates to a 7 dB loss for forward propagation only. Coaxial cables with lower electrical resistance and better RF transmission also exhibit a larger thermal conductance as a result of the Wiedemann–Franz law. We therefore selected this cable as a trade-off between RF performance and thermal load on the cryostat.

Subsequently, S_{11} was measured for the coaxial cable with flex PCB [red curve in Fig. 3(c)]. $|S_{11}|$ exhibits an overall reduced amplitude, indicating increased signal dissipation in the longer propagation path and through emission at the coil. The reflection at the internal SMA [see (1) in Fig. 3(d)] is much less pronounced. This remaining reflection is likely due to an impedance mismatch between the balun and the transmission line (see Sec. II C). The additional peak at larger delay times (2) indicates reflections at the coil (see Sec. II D).

Finally, we measured the S_{21} transmission with the flex PCB [black curve in Fig. 3(c)] by picking up the RF magnetic field with an RF magnetic field probe (Art.: TBPS01 EMC Near-field Probe H10, TekBox Digital Solutions). Note that the overall amplitude of $|S_{21}|$ depends on the spatial alignment of the field probe with the coil. The oscillations in the transmission have the same origin as the oscillations observed in the reflection measurement. $|S_{21}|$ is weighted by the response function of the magnetic field probe, causing a strong reduction in the signal intensity at low frequencies, for example. Taking the response function of the magnetic field probe into account, the signal-to-drive ratio can be derived from the S_{21} transmission, as discussed in Sec. III B.

B. Signal-to-drive characterization

For the signal-to-drive characterization, we define a frequency-dependent spectral transfer function $T(f)$ according to

$$B_\perp(t) = \Re\left\{T(f)V_{\text{source}}e^{i2\pi f t}\right\}. \tag{6}$$

The transfer function defines how the input RF signal, with amplitude V_{source}, is converted into an RF magnetic flux density $B_\perp$. $T(f)$ therefore has the dimension of magnetic flux density per voltage. $T(f)$ defined in this way captures phase delays; however, these are disregarded here.

$T(f)$ can be derived from the S_{21} transmission measurement [see Fig. 3(c)] by taking the response of the magnetic-field probe into account. This response also depends on frequency and can be described as a frequency-dependent response function $T_{\text{probe}}(f)$ such that

$$V_{\text{probe}}(t) = \Re\left\{T_{\text{probe}}(f)B_{0\perp}e^{i2\pi f t}\right\}, \tag{7}$$

where $B_{0\perp}$ is the amplitude of the sinusoidal $B_\perp(t)$. The measured probe voltage V_{probe} depends on the magnetic flux Φ that penetrates the probe scaled by the transfer function of the probe $T_{\text{probe}}(f)$. Since the magnetic flux Φ that penetrates the probe equals the average magnetic flux-density component $B_\perp$ perpendicular to the probe's loop times its area, we directly refer to $B_\perp$ for simplicity [i.e., incorporated the area in $T_{\text{probe}}(f)$].

The transfer function $T(f)$ can be obtained from the S_{21} transmission, which reflects the voltage ratio at the two ports P1 and P2

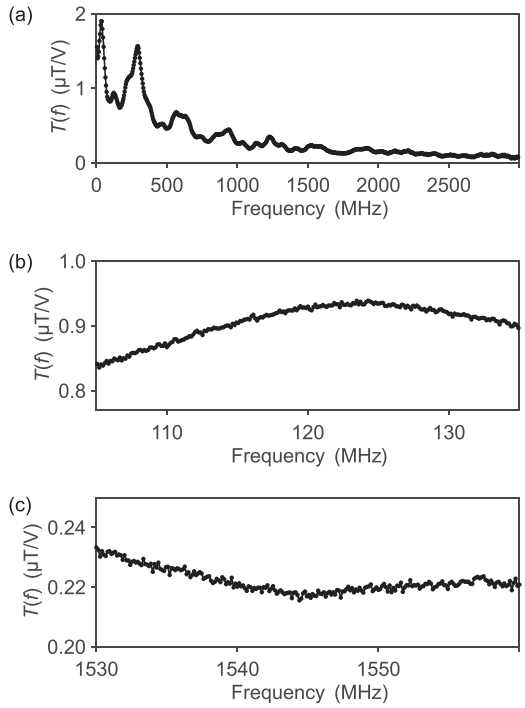

FIG. 4. (a) Spectral signal-to-drive transfer function of the RF circuit ($T(f)$), based on the transmission measurement shown in Fig. 3(c), normalized by the frequency-dependent probe response [$T_{\text{probe}}(f)$] (details provided in Sec. III B). (b) and (c) Zoomed in on selected frequency ranges corresponding to the T_x–T_y and T_x–T_z transitions of pentacene, as relevant for the ESR-AFM measurements presented in Ref. 4 and Fig. 6(a).

of the VNA [see Fig. 3(c)] as $S_{21} = V_{P2}^{in}/V_{P1}^{out}$. Given that V_{probe} is measured as V_{P2}^{in} and V_{source} is provided as V_{P1}^{out}, we obtain

$$T(f) = \frac{S_{21}}{T_{probe}(f)}. \quad (8)$$

The probe's response is specified by the manufacturer in units of output power per magnetic flux density squared, which we converted to the units of $T_{probe}(f)$ (voltage per magnetic flux density) based on the impedance of 50 Ω. The resulting $T(f)$ determined from the measured S_{21} is shown in Fig. 4(a). $T(f)$ decreases with increasing frequency, mostly owing to the limited bandwidth of the coaxial cable through the He-bath. On top of this falling trend, it shows oscillations attributed to reflections, as discussed in Sec. III A.

As indicated earlier, in ESR-AFM experiments, it is most important that resonance peak shapes, which typically extend over less than 10 MHz, are not affected by the instrument's response function. In fact, within frequency windows of about 30 MHz, no sharp resonances are observed in the spectral signal-to-drive transfer function, as illustrated in Figs. 4(b) and 4(c) for the frequency ranges used for the ESR-AFM measurements on pentacene presented in Ref. (4), with an example shown in Sec. V.

IV. MICROSTRIP SAMPLE DESIGN

To enhance the RF magnetic field at the sample surface, a microstrip sample was designed, which is shown in Fig. 5(a). A thin (i.e., 300 nm) gold structure containing a microstrip section was deposited onto a mica disk of 12 mm diameter by shadow-mask lithography. We choose to grow gold on mica since gold is known to grow epitaxially in the (111) orientation on mica surfaces.[25] The mica disk was glued onto a non-conductive spacer material and subsequently clamped onto the sample button heater.[26] We avoided a metallic support structure, since the screening with a shallow penetration depth[27] strongly suppresses RF fields above a metal.

A rendered drawing of the coil and the subjacent microstrip sample is shown in Fig. 5(b). The gold structure on the mica surface inductively picks up the primary RF magnetic field (blue) generated by the coil. We therefore also refer to the gold structure as a pick-up coil. To maximize the induced current in the pick-up coil, it has the same diameter as the coil and is placed directly beneath it. The induced current in the pick-up coil generates a secondary RF magnetic field (red), which has a particularly high magnetic flux density above the microstrip. The inset in Fig. 5(b) shows a magnified view of the microstrip. Directly above the microstrip surface, the secondary magnetic field lies in-plane [pointing along the y axis of the coordinate-system in Fig. 5(b)], whereas the primary field is perpendicular to the sample surface (pointing along the z axis), yielding two distinct components of the RF magnetic field. Assuming that the thickness of the microstrip is small compared to the width, the RF magnetic flux density directly above the microstrip, carrying the current I_{ms}, can be derived from Ampère's law as

$$B_{sec}(t) = \frac{\mu_0 I_{ms}(t)}{2w}, \quad (9)$$

where μ_0 is the magnetic permeability and w is the width of the microstrip.[21] To maximize the magnetic flux density, the microstrip

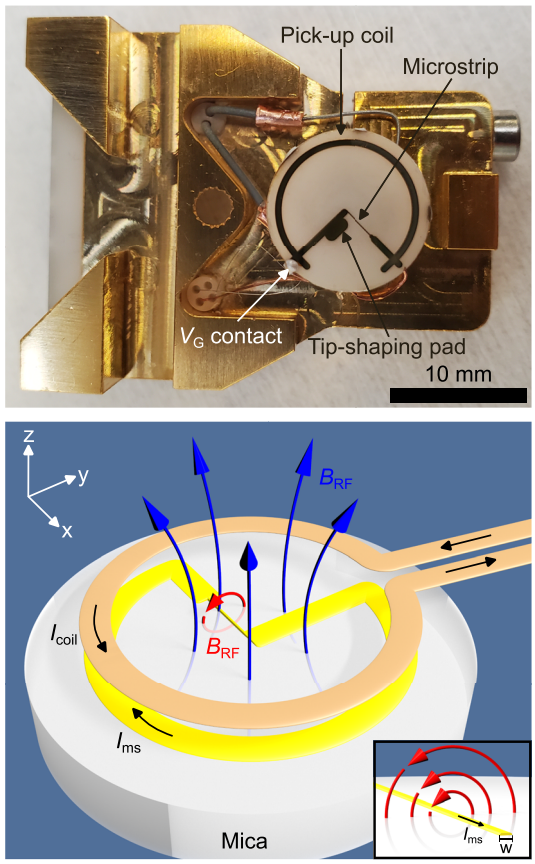

FIG. 5. Microstrip sample design. (a) Image of the sample holder with the sample. Central components are labeled. The tip-shaping pad is used for tip preparation. A copper wire is glued (electrically conductive silver epoxy, Art.: H20E, Epoxy Technology) to the gold structure to apply a gate voltage V_G as required for ESR-AFM.[4] (b) Rendered drawing of the coil and the gold structure on the sample. The RF current I_{coil} generates a primary RF magnetic field (blue). The RF signal is inductively coupled into the gold structure on the mica substrate, inducing a current I_{ms}. This current generates a secondary RF magnetic field, which is largest in the direct vicinity of the microstrip (red). The inset shows a magnified view of the microstrip of width w. The current I_{ms} generates a circular RF magnetic field around the microstrip. Directly above the microstrip, the field is pointing in-plane along the y axis.

should be as narrow as possible. However, a width of 100 μm was chosen for the practical reason to facilitate the positioning of the AFM tip. We assume that by reducing w, the signal-to-drive ratio could be increased by an order of magnitude, while still allowing the positioning of the AFM tip.

The stripline on the sample effectively enhances the magnetic field at the SPM junction, since it picks up the weaker primary magnetic field from the driving coil and generates a larger secondary magnetic field. To roughly estimate the enhancement factor, that is, the ratio of the secondary to the primary field, we use a crude approximation: The single-loop driving coil and the microstructure pick-up coil can be modeled as a 1:1 transformer with the secondary coil being shorted. Under these conditions, and neglecting losses and phase shifts, the currents in the primary and secondary circuits

are equal in magnitude. Using this rough approximation, we can directly compare the magnitude of the magnetic flux density generated at the center of the single-loop coil with that generated above the microstrip when both carry the same current $I_0 = |I_{coil}| = |I_{ms}|$, giving

$$\frac{B_{sec}}{B_{prim}} \simeq \frac{\mu_0 I_{ms}}{2w} \frac{2r_{coil}}{\mu_0 I_{coil}} = r_{coil}/w. \quad (10)$$

Although the estimate is crude and certainly not quantitatively reliable, it captures the scaling of the field enhancement. The geometry in our experiment would result in an enhancement factor of ≈50 under ideal conditions.

V. RESULTING RF MAGNETIC FIELD

The resulting RF magnetic field from the coil and microstrip can be determined from the ESR-AFM experiments presented in Ref. 4. As an example, an ESR-AFM spectrum of the T_x–T_z transition of a single pentacene molecule is shown in Fig. 6(a). Importantly, the rates of driving the spin transitions in ESR-AFM depend not only on the magnitude but also on the direction of the RF field. For driving the transitions between two of the three zero-field-split triplet states, T_x, T_y, and T_z, only the field component along one particular direction is contributing according to their selection rules.[28] The T_x–T_y transition is driven by the field component along the z axis, whereas for the T_x–T_z transition, the component along the y axis is relevant. These directions relate to the high-symmetry axes of the molecule. Consequently, the driving strength of the T_x–T_z transition depends on the in-plane orientation of the molecule with respect to the in-plane orientation of the RF field, as shown for two individual pentacene molecules in Fig. 6(b). The measured Rabi frequencies Ω reported for pentacene-d_{14} in Ref. 4 allow, therefore, determining both the orientation and the magnitude of the resulting RF field. In addition, the magnitude of the RF magnetic field can be determined from the spectral signal-to-drive transfer function (Sec. III B) and the microstrip sample enhancement factor (Sec. IV), as discussed in this section.

Note that although the pick-up coil and microstrip will affect the magnitude and orientation of the local magnetic field, they are expected not to introduce any resonances in the frequency range of interest (in windows of 10 MHz, as discussed in Sec. III). For reference, an RF signal at a frequency of 1.5 GHz (which is around the resonance frequency of the T_x–T_z transition for pentacene) has a wavelength of roughly three times the entire circumference of the loop of the pick-up coil.

A. Orientation of the in-plane RF field

The orientation of the in-plane RF field is given by the microstrip, perpendicular to the long axis of the microstrip [pointing in the y-direction in Fig. 5(b)]. For the sample used for the Rabi oscillation measurements presented in Ref. 4, this angle was (37 ± 3)° with respect to the long axis of the sample holder.

The in-plane RF field orientation can also be determined experimentally from the Rabi oscillations measured for seven pentacene-d_{14} molecules, as presented in Ref. 4. Rabi oscillations for two of these molecules (2 and 3, see Fig. 7) are shown in Fig. 6(b). The Rabi oscillation frequencies for the T_x–T_z transition for four molecules in the orientation of molecule 2 are equal within error margins, with an average of (1.90 ± 0.02) MHz (error bars represent the standard deviation). In contrast, the Rabi frequency found for three molecules in the 90° rotated adsorption geometry (orientation of molecule 3) is (0.60 ± 0.02) MHz.

To determine the exact orientation of these molecules, bond-resolved AFM images[29] were taken of the molecules for which the Rabi oscillations were measured, as exemplarily shown for molecule 2 in Fig. 7. From the orientations of the molecules and their corresponding Rabi frequencies, it follows that the magnetic RF field could either be oriented with a real-space angle of (1 ± 2)° or (36 ± 2)° with respect to the long axis of the sample holder, as indicated by the vectors in Fig. 7. This is in excellent agreement with the angle determined from the orientation of the microstrip (37 ± 3)°.

B. Magnitude of the RF field

From the spectral signal-to-drive transfer function determined in Sec. III B, the RF magnetic flux density perpendicular to the sample surface (pointing in the z-direction) for a given driving signal can be calculated. The in-plane component (pointing in the y-direction) of the RF magnetic flux density can be estimated by multiplication with the microstrip sample enhancement factor discussed in Sec. IV. The measured Rabi frequencies Ω for pentacene-d_{14} allow an independent measure of the actual magnetic flux density that was

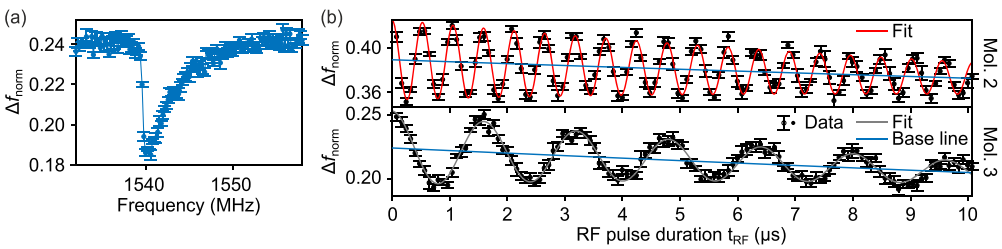

FIG. 6. (a) ESR-AFM spectrum of the T_x–T_z transition of a single pentacene-h_{14} molecule. This signal was obtained by repeated cycles of spin preparation, spin manipulation, and AFM signal readout. The experimental parameters and signal processing to obtain the normalized AFM signal Δf_{norm} are described in detail in Ref. 4. (b) Rabi oscillations of the T_x–T_z transition measured for two individual pentacene-d_{14} molecules using ESR-AFM. Molecules 2 and 3 differ in their in-plane orientation by 90° (see Fig. 7). The details of the fitting can be found in Ref. 4; the resulting RF magnetic field amplitudes are listed in Table I. Adapted from Sellies *et al.*, Nature **624**, 64 (2023). Copyright 2023 Author(s), licensed under a Creative Commons Attribution 4.0 License.

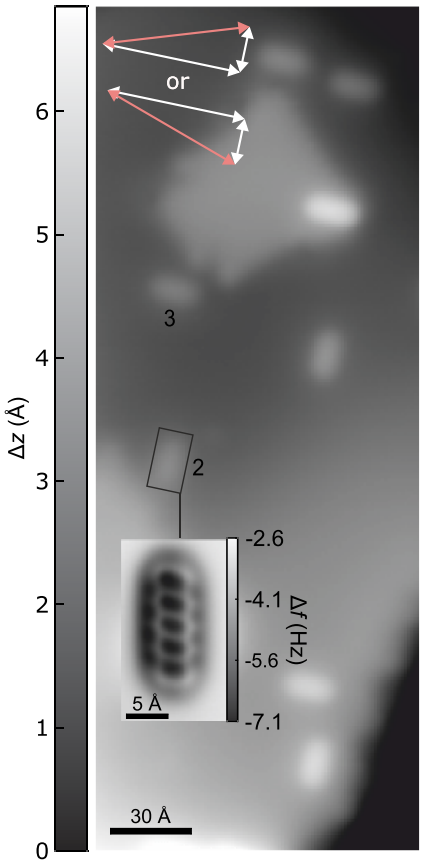

FIG. 7. AFM topography image of the NaCl-covered surface with several individual pentacene molecules measured with a CO-functionalized tip (set point: $\Delta f = -1.45$ Hz at $V = 0$ V, $A = 1.65$ Å). The length of the white arrows indicates the strength of the RF field in that direction, with their sum indicated by the pink arrows. Note that this overview image is rotated by −8° and flipped along the y axis compared to the real-space directions. The inset shows a constant-height AFM image as a close-up of molecule 2 resolving its structure ($A = 0.3$ Å, $\Delta z = -5.1$ Å with respect to the set point $\Delta f = -1.45$ Hz at $V = 0$ V, $A = 0.3$ Å). Adapted from Sellies *et al.*, Nature **624**, 64 (2023). Copyright 2023 Author(s), licensed under a Creative Commons Attribution 4.0 License.

reached. In the case of resonant spin driving, the RF magnetic flux density is given by

$$B = \frac{2\pi\Omega}{\gamma_e}, \tag{11}$$

where γ_e is the gyromagnetic ratio of the electron spin. γ_e for the triplet state of pentacene can be assumed to be equal to the one of a free electron spin. We note that the amplitudes of the magnetic flux density derived from the spectral transfer function are expected to slightly deviate from those inferred from the Rabi frequencies. This deviation can be attributed to the different damping of the RF circuit at room temperature and at 4.2 K, as well as to amplitude uncertainties associated with the field probe measurement (see Sec. III A).

TABLE I. RF magnetic flux density amplitudes calculated from the Rabi frequencies measured in Ref. 4 and shown for the T_x–T_z transition in Fig. 6(b). The Rabi oscillations were measured on pentacene-d_{14} molecules. The transition nomenclature corresponds to the three triplet spin states, T_x, T_y, and T_z.

Molecule[a]	Transition (RF freq.)	RF mag. flux dens. ampl. (μT)
2	T_x–T_y (116.8 MHz)	26
	T_x–T_z (1540 MHz)	68
3	T_x–T_y (116.9 MHz)	24
	T_x–T_z (1540.05 MHz)	21

[a]Numbering adopted from Ref. 4 and corresponding to the molecules indicated in Fig. 7.

Table I provides the flux densities calculated from the Rabi frequencies. According to the selection rules, the T_x–T_z transition depends on the in-plane orientation of the molecule. Since the two molecules listed in Table I are oriented at a 90° angle with respect to each other, a total in-plane field component of 71 μT can be extracted. The out-of-plane component can be directly inferred from the T_x–T_y transitions as 25 μT.

These field strengths can be compared to those derived from the spectral signal-to-drive transfer function. With an input voltage amplitude[30] V_{source} of 6.77 V at 117 MHz, the spectral signal-to-drive transfer function yields an RF magnetic flux density amplitude of 6 μT along the z axis, which is only about a factor of four smaller than the actual field strength obtained from the Rabi oscillations.

For the y-component of the RF magnetic flux density, the enhancement factor of the microstrip sample must be taken into account (see Sec. IV). With an input voltage amplitude V_{source} of 7.96 V, the y-component is calculated to be 102 μT, which agrees reasonably well with the value of 71 μT derived from the Rabi oscillations. We assume that for this RF frequency, the z-component of the RF field might similarly deviate by a factor of 4 at 4.2 K, while the actual microstrip sample enhancement factor might easily stay significantly below the idealized value. These two effects seem to roughly cancel each other out.

VI. SUMMARY AND OUTLOOK

In summary, we have successfully implemented a robust RF magnetic-field generation tailored for ESR-AFM measurements. Using a custom-designed flexible PCB terminated with a single-loop coil, we achieved broadband RF magnetic field generation in the low GHz range without sharp resonances. The RF circuit was experimentally characterized, and its spectral signal-to-drive transfer function was determined. Furthermore, a dedicated microstrip sample was developed to enhance the local RF magnetic field and to introduce an additional in-plane field component, enabling it to drive spin transitions that require an RF field in a specific spatial dimension.

We believe that our approach of directly introducing RF magnetic fields into the SPM setup is broadly applicable across a wide range of experiments. This method facilitates SPM experiments using non-magnetic tips, which can significantly enhance the coherence times of the investigated spin systems.

ACKNOWLEDGMENTS

We acknowledge Tobias Preis and Christoph Rohrer for their technical support and Matías Senger and Leo Gross for their discussion. Funding from the ERC Synergy Grant MolDAM (Grant No. 951519) and the Deutsche Forschungsgemeinschaft (DFG, German Research Foundation) through Grant No. RE2669/6-2 is gratefully acknowledged.

AUTHOR DECLARATIONS

Conflict of Interest

The authors have no conflicts to disclose.

Author Contributions

Raffael Spachtholz: Conceptualization (equal); Formal analysis (equal); Investigation (equal); Visualization (equal); Writing – original draft (equal); Writing – review & editing (equal). **Lisanne Sellies**: Conceptualization (equal); Formal analysis (equal); Investigation (equal); Writing – review & editing (equal). **Franziska Bruckmann**: Conceptualization (equal); Investigation (equal). **Philipp Scheuerer**: Conceptualization (equal); Investigation (equal). **Jascha Repp**: Conceptualization (equal); Investigation (equal); Supervision (equal); Writing – review & editing (equal).

DATA AVAILABILITY

The data that support the findings of this study are openly available in the University of Regensburg Publication Server at https://doi.org/10.5283/epub.78716, Ref. 31.

REFERENCES

[1] S. Baumann, W. Paul, T. Choi, C. P. Lutz, A. Ardavan, and A. J. Heinrich, Science **350**, 417 (2015).
[2] K. Yang, W. Paul, S.-H. Phark, P. Willke, Y. Bae, T. Choi, T. Esat, A. Ardavan, A. J. Heinrich, and C. P. Lutz, Science **366**, 509 (2019).
[3] Y. Wang, Y. Chen, H. T. Bui, C. Wolf, M. Haze, C. Mier, J. Kim, D.-J. Choi, C. P. Lutz, Y. Bae, S.-H. Phark, and A. J. Heinrich, Science **382**, 87 (2023).
[4] L. Sellies, R. Spachtholz, S. Bleher, J. Eckrich, P. Scheuerer, and J. Repp, Nature **624**, 64 (2023).
[5] P. Willke, W. Paul, F. D. Natterer, K. Yang, Y. Bae, T. Choi, J. Fernández-Rossier, A. J. Heinrich, and C. P. Lutz, Sci. Adv. **4**, eaaq1543 (2018).
[6] T. S. Seifert, S. Kovarik, C. Nistor, L. Persichetti, S. Stepanow, and P. Gambardella, Phys. Rev. Res. **2**, 013032 (2020).
[7] C. A. Hutchison, Jr. and B. W. Mangum, J. Chem. Phys. **29**, 952 (1958).
[8] F. Gerson and W. Huber, *Electron Spin Resonance Spectroscopy of Organic Radicals* (John Wiley & Sons, 2003).
[9] W. Paul, S. Baumann, C. P. Lutz, and A. J. Heinrich, Rev. Sci. Instrum. **87**, 074703 (2016).
[10] Y. Chen, Y. Bae, and A. J. Heinrich, Adv. Mater. **35**, 2107534 (2023).
[11] J. Lee, X. Tu, and W. Ho, Nano Lett. **5**, 2613 (2005).
[12] R. Giridharagopal, J. Zhang, and K. F. Kelly, Rev. Sci. Instrum. **82**, 053710 (2011).
[13] M. Poggio, C. L. Degen, C. T. Rettner, H. J. Mamin, and D. Rugar, Appl. Phys. Lett. **90**, 263111 (2007).
[14] B. C. Stipe, H. J. Mamin, C. S. Yannoni, T. D. Stowe, T. W. Kenny, and D. Rugar, Phys. Rev. Lett. **87**, 277602 (2001).
[15] D. Rugar, C. S. Yannoni, and J. A. Sidles, Nature **360**, 563 (1992).
[16] H. J. Mamin, R. Budakian, and D. Rugar, Rev. Sci. Instrum. **74**, 2749 (2003).
[17] K. Besocke, Surf. Sci. **181**, 145 (1987).
[18] G. Meyer, Rev. Sci. Instrum. **67**, 2960 (1996).
[19] F. J. Giessibl, Rev. Mod. Phys. **75**, 949 (2003).
[20] T. H. Lee, *Planar Microwave Engineering* (Cambridge University Press, 2004).
[21] R. Serway and J. Jewett, *Physics for Scientists and Engineers with Modern Physics* (Cengage Learning, 2014).
[22] S. Y. Kilin, A. P. Nizovtsev, P. R. Berman, C. Von Borczyskowski, and J. Wrachtrup, Phys. Rev. B **58**, 8997 (1998).
[23] W. Steurer, S. Fatayer, L. Gross, and G. Meyer, Nat. Commun. **6**, 8353 (2015).
[24] J. Schmidt and J. H. Van der Waals, Chem. Phys. Lett. **3**, 546 (1969).
[25] C. E. D. Chidsey, D. N. Loiacono, T. Sleator, and S. Nakahara, Surf. Sci. **200**, 45 (1988).
[26] Sample button heater from CreaTec Fischer & Co. GmbH Art.: LT-STM-Z0002; Macor is used as a spacer material between the mica disk and the sample button heater. The mica is glued using small dots of silver epoxy.
[27] Z. Mottl, NDT Int. **23**, 11 (1990).
[28] R. W. Brandon, R. E. Gerkin, and C. A. Hutchison, Jr., J. Chem. Phys. **41**, 3717 (1964).
[29] L. Gross, F. Mohn, N. Moll, P. Liljeroth, and G. Meyer, Science **325**, 1110 (2009).
[30] Amplitude is used to mean peak amplitude.
[31] R. Spachtholz, L. Sellies, F. Bruckmann, P. Scheuerer, and J. Repp, Data archive of "Implementation of radio-frequency magnetic fields for electron spin resonance in a low-temperature atomic force microscope," University of Regensburg Publication Server, 2026, https://doi.org/10.5283/epub.78716.